



# Synthesis of a novel magnetic SnNb<sub>2</sub>O<sub>6</sub>/CoFe-LDH 2D/2D heterostructure for the degradation of organic pollutants under visible light irradiation

Jun Liu<sup>1</sup> , Jia Li<sup>1,\*</sup> , Longxin Wang<sup>1</sup> , Xingmei Bing<sup>1</sup> , Xinling Cui<sup>1</sup> , Fei Ji<sup>1</sup> , and Denis Diengula Kionga<sup>1</sup>

<sup>1</sup> School of Material Science and Engineering, University of Jinan, Jinan, China

Received: 1 May 2018

Accepted: 12 August 2018

Published online:  
22 August 2018

© Springer Science+Business  
Media, LLC, part of Springer  
Nature 2018

## ABSTRACT

A novel two-dimensional/two-dimensional (2D/2D) magnetic SnNb<sub>2</sub>O<sub>6</sub>/CoFe-LDH hybrid was first prepared via a simple hydrothermal assembly method. The SnNb<sub>2</sub>O<sub>6</sub>/CoFe-LDH heterostructures displayed distinctly enhanced photocatalytic ability toward Methyl orange (MO), which was about 1.1 and 1.2 times higher than that of SnNb<sub>2</sub>O<sub>6</sub> and CoFe-LDH, respectively. It is believed that the improved photocatalytic performance was mainly due to the unique energy band structure of heterostructures, which facilitated the efficient separation and transfer of photoinduced carriers and enhanced light harvesting. Moreover, the obtained photocatalyst exhibited high magnetic response under an external magnetic field, which was beneficial to the recovery of SnNb<sub>2</sub>O<sub>6</sub>/CoFe-LDH from aqueous solution. The successful fabrication of a visible-light-driven magnetic 2D/2D heterostructure photocatalyst is a significant contribution to wastewater treatment.

## Introduction

Environment pollution and energy crisis have been attracting intense research interest due to their great harm to human health and environment. Conventional treatment or biodegradation for environment remediation were found inefficient and may cause secondary pollution, while sunlight-driven semiconductor based photocatalyst system is considered as one of promising strategies due to direct conversion of solar energy into chemical usable energy with non-

polluting [1–4]. To date, various types of semiconductors such as metal oxides, sulfides, and nitroxide were successfully synthesized and found to be active photocatalysts with universal applications [5–8].

Foordite SnNb<sub>2</sub>O<sub>6</sub>, as a typical layered niobate, has been undergoing fast development in the domain of photocatalysis for the advantages of facile preparation, unique energy band structure, low cost, superior catalytic, and stability [9, 10]. SnNb<sub>2</sub>O<sub>6</sub> consists of sheets with two-octahedron-thick, which insert edge-sharing octahedral NbO<sub>6</sub> units and Sn<sup>2+</sup> ions. For electronic band structure of SnNb<sub>2</sub>O<sub>6</sub>, the hybrid

Address correspondence to E-mail: mse\_lij@ujn.edu.cn

orbitals of Sn 5s and O 2p are responsible to the valence band that makes photocatalytic under visible light possible [11]. However, the large-scale application of SnNb<sub>2</sub>O<sub>6</sub> is still limited due to its low catalytic efficiency resulted from low surface area and short life of charge carriers. SnNb<sub>2</sub>O<sub>6</sub>-based composites have been prepared by constructing heterojunctions or loading co-catalyst to improve the photocatalytic ability of pure SnNb<sub>2</sub>O<sub>6</sub>. Jin et al. [12] have successfully synthesized TiO<sub>2</sub>-SnNb<sub>2</sub>O<sub>6</sub> heterojunctions, which exhibits significantly improved photocatalytic degradation toward RhB ascribed to improve charge transfer efficiency and suppress carriers recombination. Zhang et al. [13] have developed novel SnNb<sub>2</sub>O<sub>6</sub>/g-C<sub>3</sub>N<sub>4</sub> 2D/2D nanosheet heterostructures, which exhibits excellent photocatalytic ability to photodegrade MB which is attributed to strong interfacial interaction and efficient charge separation. Among these heterojunctions, 2D/2D nanostructure has been found a promising system for further enhancement in photocatalytic performance. According to recent reports, 2D/2D semiconductor structure with strong electronic and physical coupling effect and extend contact area is beneficial for transferring of charge carriers and suppressing the electron–hole pairs recombination, which resulted in remarkable improved in the photocatalytic ability [14–16].

Recently, layered double hydroxides (LDHs) have attracted great interest for various applications in environmental remediation due to the exchangeability of interlayer anions and the superior adsorption ability [17–19]. Specifically, the edge sites of LDHs are rich in open coordination, which could act as active adsorption sites for pollutants [20]. For LDH-based photocatalysts, the good adsorption capacity of LDH can increase the concentration of pollutants around the photocatalysts, which can improve the photocatalytic efficiency of LDH-based photocatalysts. In addition, LDHs with magnetic components like transition metals can be easily recovered by an external magnetic field [21]. Magnetic adsorption separation technology has been widely applied in environment purification applications [22]. For magnetic photocatalysts, it is easily separated and reclaimed by a simple magnetic separation process after reaction, avoiding recontamination in water remediation. CoFe-LDH exhibits both great magnetic response and catalytic performance, which has triggered great attention of scientists [23–25]. Besides, the

Co and Fe elements existing together can provide rich redox reactions that are beneficial to promote the process of reaction [26].

In this paper, for the first time, we designed and constructed a new 2D/2D magnetic nanosheets SnNb<sub>2</sub>O<sub>6</sub>/CoFe-LDH heterostructure (Scheme 1) by a simple hydrothermal co-assembly method. The organic dyes, methyl orange (MO), were selected as model pollutants to evaluate the photocatalytic performance of as-synthesized composites under simulate visible light. It was demonstrated that SnNb<sub>2</sub>O<sub>6</sub>/CoFe-LDH displayed enhanced ability of photodegrading organic pollutants compared to pure SnNb<sub>2</sub>O<sub>6</sub> and CoFe-LDH nanosheets. Besides, the as-prepared magnetic catalyst exhibited quickly magnetic response under an external magnetic field and thus could be easily recovered after wastewater treatment. Furthermore, a possible photocatalytic mechanism was proposed based on the experimental results.

## Experimental

### Reagents

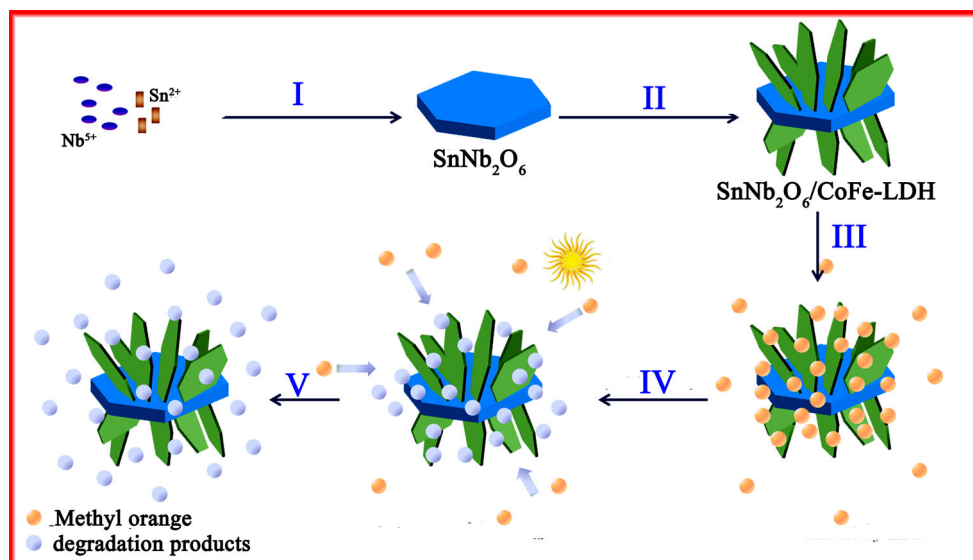
Niobium(V) oxide (Nb<sub>2</sub>O<sub>5</sub>), hydrochloric Acid (HCl), and iron (III) chloride hexahydrate (FeCl<sub>3</sub>·6H<sub>2</sub>O) were purchased from Guang Cheng Chemical Reagents (Tianjin, China). Potassium hydroxide (KOH) and sodium hydroxide (NaOH) were purchased from Dengke Chemical Reagents (Tianjin, China). Iron (III) nitrate nonahydrate (Fe(NO<sub>3</sub>)<sub>3</sub>·9H<sub>2</sub>O), cobalt chloride hexahydrate (CoCl<sub>2</sub>·6H<sub>2</sub>O), ferrous chloride (FeCl<sub>2</sub>), ethylene-diamine tetraacetic acid (C<sub>10</sub>H<sub>16</sub>N<sub>2</sub>O<sub>8</sub>), stannous chloride dihydrate (SnCl<sub>2</sub>·2H<sub>2</sub>O), anhydrous ethanol, and 1,4-benzoquinone (C<sub>6</sub>H<sub>4</sub>O<sub>2</sub>) were purchased from Sinopharm Group Chemical Reagent Co., Ltd (China). Methyl orange (C<sub>14</sub>H<sub>14</sub>N<sub>3</sub>NaO<sub>3</sub>S) and isopropanol (C<sub>3</sub>H<sub>8</sub>O) were purchased from Tianjin Kemiou Chemical Reagent Co., Ltd (China). In the experiments, deionized water (DI) was used and all chemicals were analytical grade.

### Preparation of SnNb<sub>2</sub>O<sub>6</sub> and SnNb<sub>2</sub>O<sub>6</sub>/CoFe-LDH

In this work, pure SnNb<sub>2</sub>O<sub>6</sub> (abbreviated as SNO) nanosheet was synthesized by a two-step hydrothermal method as reported formerly [27].

**Scheme 1** Schematic illustration of the fabrication route and photocatalytic performance of hybrid  $\text{SnNb}_2\text{O}_6/\text{CoFe-LDH}$  nanocomposites.

(I) Hydrothermal synthesis at 200 °C for 48 h; (II) adding  $\text{Co}^{2+}$  and  $\text{Fe}^{3+}$  by hydrothermal co-assembly synthesis at 130 °C for 24 h; (III) Methyl orange enrichment around catalysts; (IV) process of adsorption and photocatalytic MO under visible light; (V) photodegradation MO.



Briefly, at first, a precursor  $\text{Nb}_2\text{O}_5 \cdot n\text{H}_2\text{O}$  was obtained from a simple procedure by dispersing  $\text{Nb}_2\text{O}_5$  (1 g) and KOH (4.48 g) into 70 mL deionized water under stirred. Then, the mixture solution was transferred into a Teflon-lined vessel (100 mL) at 200 °C for 48 h. After that, the pH of suspension was maintained at 7 by using HCl (2 mol  $\text{L}^{-1}$ ) to obtain precursor ( $\text{Nb}_2\text{O}_5 \cdot n\text{H}_2\text{O}$ ). Secondly,  $\text{SnCl}_2 \cdot 2\text{H}_2\text{O}$  (0.84 g) was added into the above solution and then adjusted the pH of the mixture to 2 by using HCl (2 mol  $\text{L}^{-1}$ ) under continuously stirred. Finally, the obtained suspension was heat-treated at 200 °C for 36 h by using a 100-mL Teflon-lined vessel. After cooled naturally, the precipitate was collected by centrifuge and washed 3 times with DI water and anhydrous ethanol, and then dried at 80 °C (8 h).

$\text{SnNb}_2\text{O}_6/\text{CoFe-LDH}$  was fabricated by a hydrothermal assembly reaction.  $\text{CoCl}_2 \cdot 6\text{H}_2\text{O}$  (0.16 M) and  $\text{Fe}(\text{NO}_3)_3 \cdot 9\text{H}_2\text{O}$  (0.055 M) were dissolved in DI water (30 mL) to form a uniform solution. After that, added  $\text{SnNb}_2\text{O}_6$  (0.5 g) into the above solution and adjusted the pH values of mixture to 9 by NaOH (1 M) under continuous magnetic stirring. Then transferred the solution into a Teflon-lined vessel (100 mL) and heat-treated at 120 °C for 20 h. Finally, samples were washed several times and then dried at 60 °C for 12 h.

### Characterization

The purity of the phases was investigated by X-ray diffraction (XRD, Bruker D8-Advance, Cu  $K\alpha$  radiation). Field emission scanning electron microscopy (FESEM, FEI QUANTA FEG250, USA) and high-resolution transmission electron microscopy (HRTEM, TecnaiF20, Philips, Hillsboro, OR, USA) were used to check the morphology of photocatalysts, while the composition was examined by energy-dispersive X-ray spectrometry (EDS, INCA Energy 3294). The optical property was studied by UV-Vis diffuse reflectance adsorption (Shimadzu UV-3600 spectrometer) in the wavelength number region of 200–800 nm. Surface elemental composition and state were measured by X-ray photoelectron spectra (XPS). Fourier transform infrared (FTIR) spectra analysis was performed on a Nicolet 380 spectrometric analyzer. The surface area and corresponding pore-sized distribution of samples were calculated by the Brunauer–Emmett–Teller (BET) model and Barrett Joyner Halenda (BJH) theory. The alternating gradient magnetometer (AGM) was used to test the magnetic property of samples. The total organic carbon (TOC) concentration was determined by Vario TOC (Elementar Company, Germany). The photoluminescence (PL) spectra were obtained by an F-4600 Flspectrophotomet with excitation energy of 360 nm.

## Batch adsorption experiments

Adsorption kinetics experiments and equilibrium experiments were conducted to test the adsorption capacity of the obtained samples toward methyl orange (MO) at room temperature. In the adsorption kinetics experiments, 50 mg adsorbents were added into 50 mL MO solution ( $30 \text{ mg L}^{-1}$ ) for adsorption reaction. At appropriate time intervals, the concentration of MO was measured by UV–Vis spectroscopy (at  $\lambda_{\text{max}} = 463 \text{ nm}$ ) after centrifuged at 6000 rpm for 5 min. For isotherm experiments, 50 mg adsorbents were added into MO aqueous solutions with different concentrations ( $25\text{--}50 \text{ mg L}^{-1}$ ) for 72 h until reached equilibrium. After adsorption process, the residual dye concentration was also measured by UV–Vis spectroscopy.

The adsorption content of MO was calculated using the following formula [28]:

$$q_t = \frac{(C_0 - C_t) \times V}{m} \quad (1)$$

where  $C_0$  ( $\text{mg L}^{-1}$ ) and  $C_t$  ( $\text{mg L}^{-1}$ ) are the initial and at time  $t$  (min) concentration of MO, respectively.  $V$  (L) is the MO solution volume,  $q_t$  ( $\text{mg g}^{-1}$ ) is the amount of adsorbate at sorption time  $t$  (min) and  $m$  (g) is the adsorbent weight.

## Photocatalytic measurements

The typical photodegradation MO dye experiments were conducted to estimate the photocatalytic performance of the obtained samples. A 500-W Xenon lamp (GXH500, Shanghai Jiguang Co., Ltd.) was used to simulate visible light irradiation source to trigger the photocatalytic reaction. Fifty milligrams of photocatalysts was placed in 80 mL MO solution ( $30 \text{ mg L}^{-1}$ ) and stirred in the darkness for 30 min before irradiation. After achieved equilibrium of adsorption–desorption, photocatalytic reaction was initiated by switched on the Xenon lamp for 1 h. During the reaction, 4.0 mL solution was withdrawn from the dye solution by a centrifuge at the preset time interval (10 min). Afterward, the concentration of MO solution was analyzed by UV–Vis spectrophotometer, and the characteristic absorption peak of MO is 463 nm.

## Results and discussion

### Characterization of samples

The phase and composition of as-prepared SNO, CoFe-LDH and SNO/CoFe-LDH heterostructure were characterized by X-ray diffraction test. As shown in Fig. 1a, the peaks collected from the SNO and CoFe-LDH matched well with the  $\text{SnNb}_2\text{O}_6$  (JCPDS card No. 84-1810) and CoFe-LDH (JCPDS card No. 50-0235), respectively. For the SNO sample, the main diffraction peaks at about  $24.9^\circ$ ,  $29.0^\circ$ ,  $31.3^\circ$ ,  $33.8^\circ$ , and  $36.9^\circ$  corresponded to the diffractions of  $(-111)$ ,  $(311)$ ,  $(600)$ ,  $(202)$ , and  $(020)$  planes, respectively [13]. As for the pristine CoFe-LDH, the XRD pattern exhibits three diffraction peaks at  $11.6^\circ$ ,  $23.4^\circ$ , and  $35.1^\circ$  assigned to the  $(003)$ ,  $(006)$ , and  $(009)$  crystal planes, respectively, which confirmed the successful fabrication of LDH structure [29]. Besides, the value of  $(003)$  plane was 0.76 nm, which revealed the presence of carbonate ions between the interlayers of LDH [30]. The XRD pattern of SNO/CoFe-LDH composite, as shown in curve c, indicated a combination of SNO and LDH with no other obvious impurity phases. Thus, it can be inferred that the high-purity SNO/LDH nanosheets heterojunction was successfully synthesized. The functional groups presented in the samples were examined by FTIR, as shown in Fig. 1b. The broad adsorption band at  $3440 \text{ cm}^{-1}$  was due to the -OH stretching vibration. The absorption bands at  $1635 \text{ cm}^{-1}$  and  $1379 \text{ cm}^{-1}$  were assigned to the presence of interlayer water molecules and the typical vibration of carbonate species, respectively [31, 32]. At the low wave numbers, the peak of LDH at  $1034 \text{ cm}^{-1}$  was the characteristic of  $\text{CO}_3^{2-}$ , which further confirmed the presence of  $\text{CO}_3^{2-}$  in the interlayer of LDH [33, 34]. Additionally, the typical stretching vibration absorptions of M–OH and M–O (M=Co, Fe) were responsible for the lower wavenumbers region  $< 800 \text{ cm}^{-1}$  [35]. For SNO, the peaks at 670 and  $480 \text{ cm}^{-1}$  were attributed to the typical internal Nb–O stretching vibration in the  $\text{NbO}_6$  octahedron [36]. Compared with the spectra of SNO and CoFe-LDH, the main peaks of SNO/CoFe-LDH can be easily assigned. However, the adsorption bands of CoFe-LDH were narrow and weak due to the low amounts of LDH in the synthesized SNO/CoFe-LDH.

The morphologies and surface structures of the catalysts were investigated by FESEM. As shown in

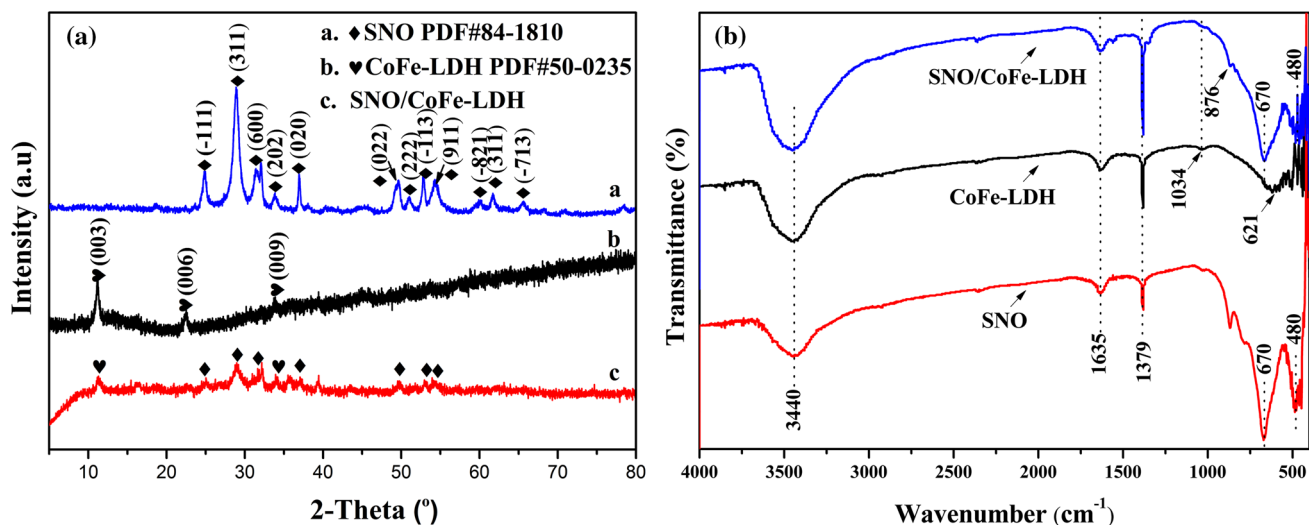


**Figure 1** XRD patterns of SNO, CoFe-LDH and SNO/CoFe-LDH heterostructure (a). FTIR spectra of SNO, CoFe-LDH and SNO/CoFe-LDH heterostructure (b).

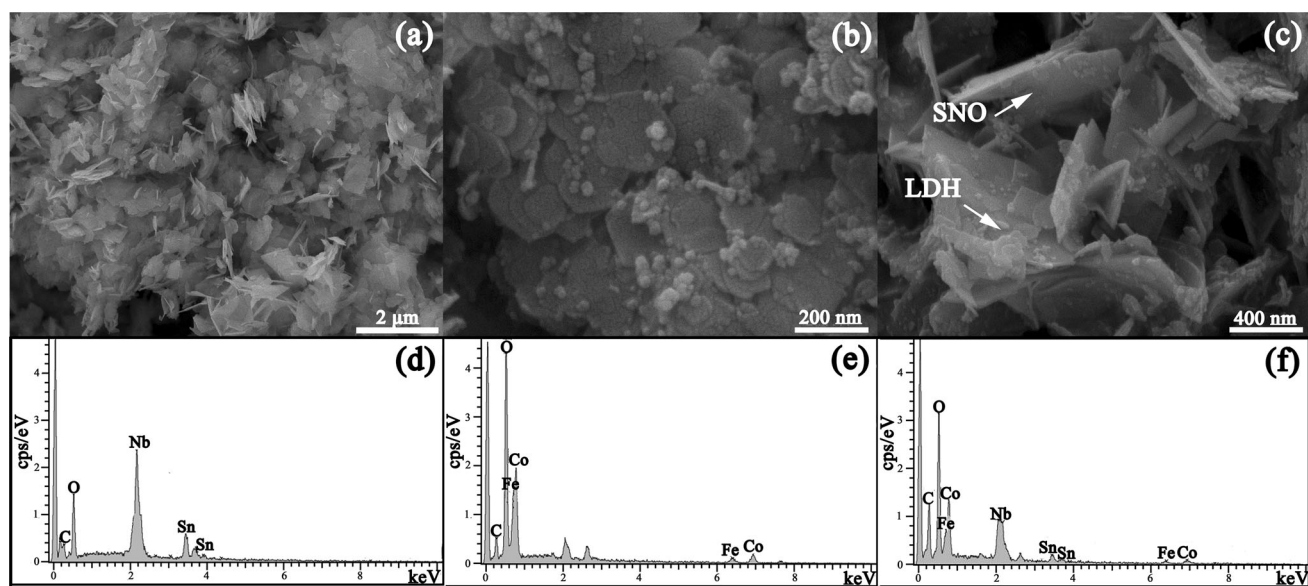


**Figure 2** FESEM images and EDS patterns of SNO (a, d), CoFe-LDH (b, e) and SNO/CoFe-LDH heterostructure (c, f).

Fig. 2a, SNO was irregular nanosheets with square-like shape. For the CoFe-LDH, irregular nanoplates containing some small nanoplatelets can be observed in the image Fig. 2b. After hydrothermal synthesis, it can be seen that SNO/CoFe-LDH was composed of SNO nanosheets and LDH nanoplates, which was consistent with the above XRD results. As shown in Fig. 2c, LDH nanosheet grew anisotropically on the surface of SNO to form a 2D–2D structure, which can expose more active sites and facilitate the photocatalytic reaction [37]. The EDS patterns demonstrate that SNO was mainly composed of Sn, Nb and O

elements (Fig. 2d), while LDH was composed of Co, Fe, C and O elements (Fig. 2e). No other elements were detected from Fig. 2f, indicating that the as-synthesized heterostructure consisted of SNO and LDH. Combining with the above-mentioned results, therefore, it could be deduced that pure SNO, CoFe-LDH, and SNO/CoFe-LDH were successfully fabricated.

To further explore the detail structure characteristics of the obtained samples, TEM analysis was carried out. Figure 3a displays the TEM image of the pure SNO. It reveals that SNO was thin lamellar

nanosheets with lateral dimensions around hundreds of nanometers. As can be seen in Fig. 3b, CoFe-LDH was composed of irregular nanoplatelets and nanoplates with the width of approximately 200 nm. Figure 3c shows that the LDH nanosheets were successfully covered on the surface of SNO ultrathin nanosheets, and this 2D–2D structure maintained throughout the whole synthesis process.

$N_2$  adsorption–desorption measurement was carried out to analyze the specific surface area and the corresponding pore characteristic of the samples. Figure 4a shows that the isotherms of all samples corresponded well to the type IV isotherm with a typical  $H_3$  hysteresis loop, indicating the coexistence of micropores and mesopores in the obtained samples [13, 38, 39]. The BET surface areas of SNO, CoFe-LDH and SNO/CoFe-LDH were determined to be ca. 46.12, 61.59, and 55.57  $m^2 g^{-1}$ , and the pore volumes were calculated to be 0.281, 0.143, and 0.261  $cm^3 g^{-1}$ , respectively. Besides, as shown in Table 1, the average pore diameters of SNO, CoFe-LDH and SNO/CoFe-LDH were 24.42, 26.79 and 18.75 nm, respectively, suggesting that they were all mesoporous materials [13]. The chemical structures and elements states of catalysts were characterized by XPS (Fig. 4b–h). For CoFe-LDH, C 1s XPS spectrum displays the prominent peak at binding energy of 284.6 eV, which was assigned to the aromatic linked carbon (C=C). Another peak located at 288.2 eV was due to carboxylate carbon (O–C=O) derived from the carbonate of interlayer (Fig. 4b) [40, 41]. For the Co 2p high-resolution XPS spectrum (Fig. 4c), the peaks of Co 2p<sub>1/2</sub> (796 eV) and Co 2p<sub>3/2</sub> (780 eV) with the latter accompanied by satellites bands at 802 eV and

**Figure 4**  $N_2$  adsorption–desorption isotherms of SNO, CoFe-LDH and SNO/CoFe-LDH (a), and the corresponding pore size distributions (inset of a), XPS spectra of C 1s (b), Co 2p (c), Fe 2p (d), Nb 3d (e), O 1s (f), Sn 3d (g) and the full spectrum survey of SNO/CoFe-LDH (h).

786 eV were observed, respectively, demonstrating that the  $Co^{2+}$  was existed [26]. In the case of Fe 2p spectrum (Fig. 4d), we noted that the Fe 2p<sub>1/2</sub> and Fe 2p<sub>3/2</sub> spin–orbit splitting values were located at 724.5 eV and 715.5 eV, respectively, indicating that the existence of the  $Fe^{3+}$  in the LDH [42]. In Fig. 4e, the binding energies located at 209.47 eV and 206.47 eV corresponded to Nb 3d<sub>3/2</sub> and Nb 3d<sub>5/2</sub>, respectively, suggesting that the  $Nb^{5+}$  oxidation state was existed in SNO [43]. O 1s spectrum of SNO shows two peaks centered at 531.1 eV and 539.9 eV, demonstrating that the chemical state of O element was  $O^{2-}$  (Fig. 4h) [11]. Besides, the peaks located at 494.57 eV and 486.17 eV were assigned to the Sn 3d<sub>3/2</sub> and Sn 3d<sub>5/2</sub> (Fig. 4g), respectively, indicating that the chemical state of Sn in the SNO was  $Sn^{2+}$  [44]. Meanwhile, the XPS survey spectrum shows the peaks of Co, Fe, C, Nb, Sn and O, which was inconsistent with the elements in SNO/CoFe-LDH heterojunctions (Fig. 4h).

UV–Vis diffuse reflectance spectra with the range of 200–800 nm was carried out to characterize the optical properties of synthesized samples (Fig. 5a). Pure SNO and LDH all exhibited visible light absorption. The visible light absorption ability of LDH/SNO composite was greatly enhanced, and the intensity of absorption was higher than that of blank SNO and LDH. The enhanced light adsorption can

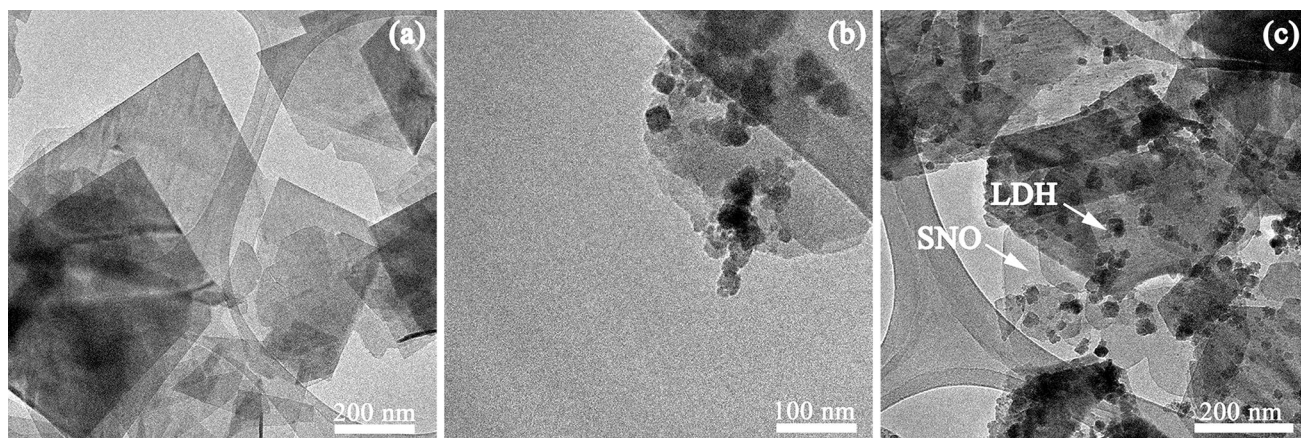
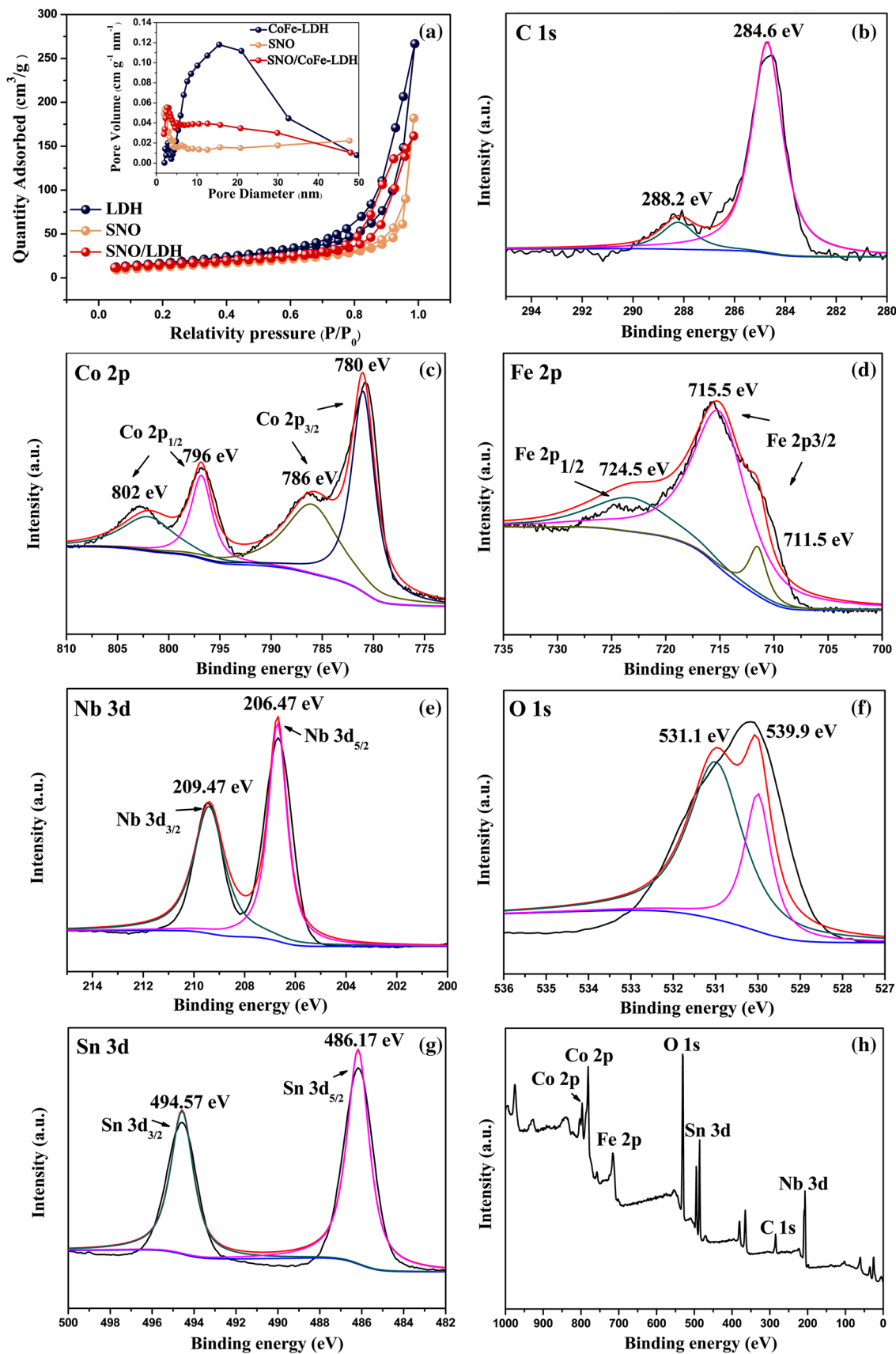


**Figure 3** TEM images of SNO (a), CoFe-LDH (b) and SNO/CoFe-LDH heterostructure (c).



generate more photogenerated electron–hole pairs and thus improve the photocatalytic activity [45].

The following formula can be used to calculate the energy bandgap of photocatalysts [46]:

$$(\alpha h\nu)^{1/n} = A(h\nu - E_g) \tag{2}$$

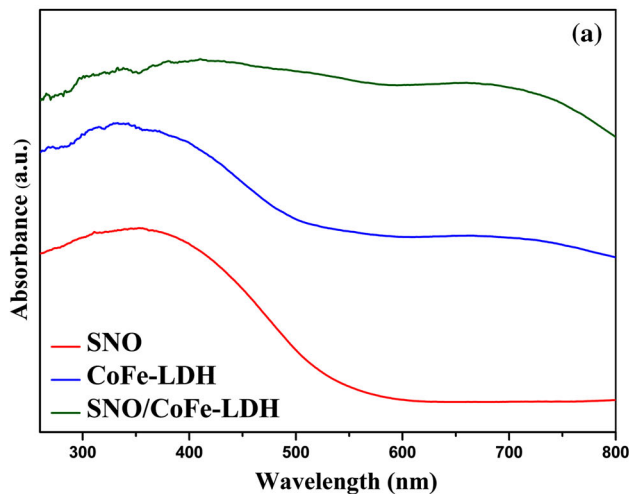
where  $\alpha$ ,  $h$  and  $\nu$  are absorption coefficient, Planck’s constant and light frequency, respectively.  $E_g$  is the bandgap energy and  $A$  is a constant [46–48]. The value of  $n$  is 2 means direct transition of a semiconductor, while  $n$  is 1/2 means indirect transition [46]. For SNO and LDH, the values of  $n$  are both of 2. As can be seen from Fig. 5b, the estimated bandgap energies were 2.18 eV and 2.53 eV corresponding to CoFe-LDH and SNO, respectively. The energy band structure of photocatalysts can be obtained from the following formula [49]:

$$E_{VB} = \chi - E^c + 0.5E_g \tag{3}$$

$$E_{CB} = E_{VB} - E_g \tag{4}$$

**Table 1** Pore texture parameters of the SNO, CoFe-LDH and SNO/CoFe-LDH

Sample	Surface area (m <sup>2</sup> g <sup>-1</sup> )	Pore volume (cm <sup>3</sup> g <sup>-1</sup> )	Average pore size (nm)
SNO	46.12	0.281	24.42
CoFe-LDH	61.59	0.143	26.79
SNO/CoFe-LDH	55.57	0.261	18.75



where the  $E_{VB}$  and  $E_{CB}$  stand for the energy of valence band (VB) and conduction band (CB), respectively.  $X$  means the absolute electronegativity of SNO and CoFe-LDH, which are 4.81 eV and 4.275 eV, respectively [27].  $E^c$  is around 4.5 eV and  $E_g$  stands for the energy of bandgap. The VB and CB values of SNO were calculated to be 1.57 eV and - 0.96 eV, respectively, while those for CoFe-LDH were 0.86 eV and - 1.32 eV, respectively.

**Adsorption studies**

Kinetics models were carried out to investigate the adsorption mechanisms. Figure 6a shows the relationship between contact time and the amount of MO adsorption. The MO adsorption amounts of SNO, LDH, and SNO/LDH were up to 3.66, 21.19, and 26.26 mg g<sup>-1</sup> after adsorption equilibrium, respectively. SNO/LDH exhibited better adsorption capacity than pure SNO and LDH. Furthermore, the removal rates were found to be rapid initially due to the mass accessible reaction sites, and then gradually slowed until reached equilibrium, suggesting that the adsorption process might include intraparticle diffusion and external mass transfer [50]. Furthermore, two kinetic models were used to analyze the adsorption mechanism. Pseudo-first-order kinetic expression can be expressed as follows [51]:

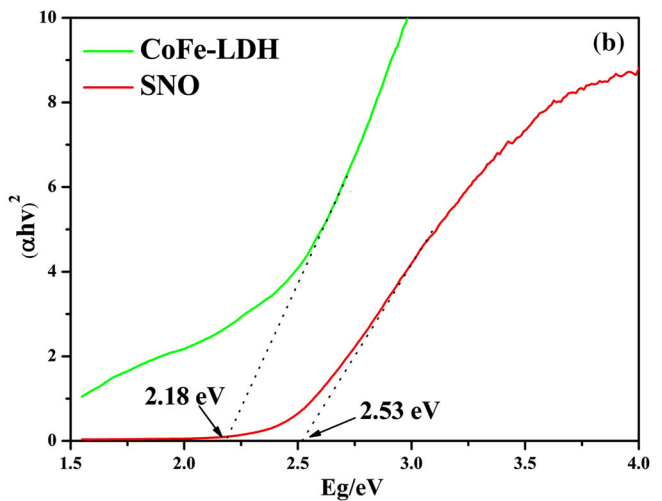


**Figure 5** UV–Vis diffuse reflectance spectra of SNO, CoFe-LDH and SNO/CoFe-LDH (a), and plot of  $(\alpha h\nu)^2$  versus  $E_g$  for the bandgap energy of SNO, CoFe-LDH (b).



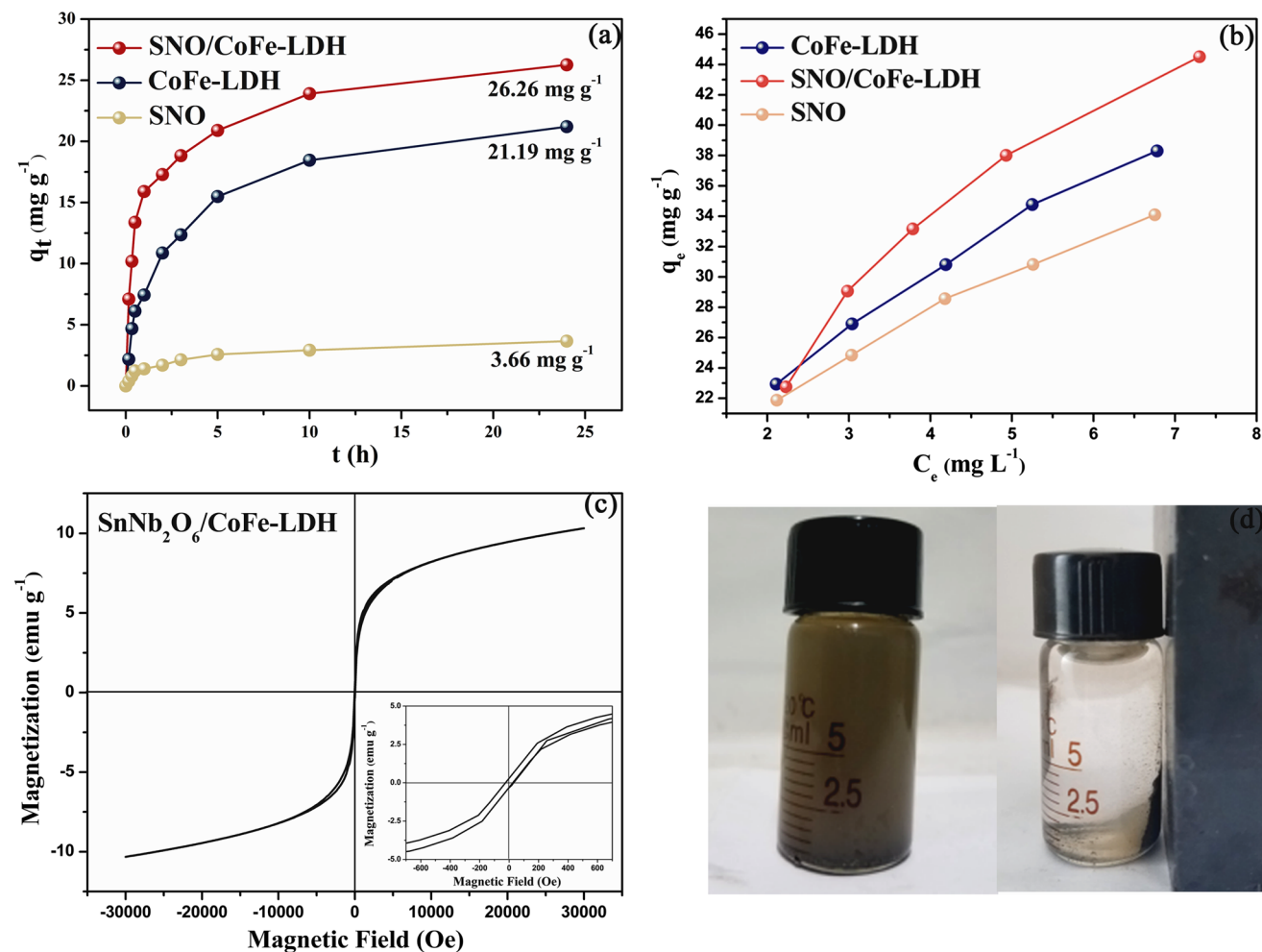


**Figure 6** Sorption capacity versus time plots (a) and isotherms of MO adsorption on as-obtained catalysts (b). Magnetization curves of SNO/CoFe-LDH (c) and the corresponding photograph of magnetic separation with a permanent magnet (d).

$$\frac{dq_t}{dt} = kt(q_e - q_t) \quad (5)$$

The experiments kinetic data can be intended by the integrating Eq. (5) [52]:

$$\ln \frac{(q_e - q_t)}{q_e} = -k_1 t \quad (6)$$

where  $k_1$  (h<sup>-1</sup>) and  $t$  (h) are the sorption rate constant and the sorption time, respectively. Besides,  $q_t$  (mg g<sup>-1</sup>) is the adsorption amount at time  $t$  and  $q_e$  (mg g<sup>-1</sup>) is the capacity of adsorption at equilibrium.

The pseudo-second-order kinetic can be expressed by the following form [52]:

$$dq_t/dt = k_2(q_e - q_t)^2 \quad (7)$$

The linear equation of pseudo-second-order was used for analyzing kinetic data [52]:

$$1/q_t = 1/k_2 q_e^2 + t/q_e \quad (8)$$

where  $k_2$  (g mg<sup>-1</sup> h<sup>-1</sup>) stands for the rate constant of adsorption in the adsorption process.

Figure S1 displays the fitted plots corresponding to two adsorption kinetics, and the related adsorption kinetics parameters are presented in Table S1. The adsorption process can be described well by pseudo-second-order kinetic model due to the high correlation coefficient  $R^2$ , which suggested that the MO adsorption of MO on the obtained samples depended both on the concentration of adsorbate and adsorbent [50].

Langmuir model and Freundlich model were used to further investigate the adsorption mechanism and the interaction between adsorbate and adsorbent. Langmuir model is based on the assumption that monolayer adsorption with identical adsorption sites

occurs on the surface of adsorbents, which can be expressed as follow [51]:

$$\frac{C_e}{q_e} = \frac{1}{q_{\max}K_L} + \frac{C_e}{q_{\max}} \quad (9)$$

where  $q_{\max}$  ( $\text{mg g}^{-1}$ ) and  $K_L$  ( $\text{L mg}^{-1}$ ) are the maximum adsorption amount of adsorbate and the Langmuir constant, respectively.  $R_L$  stands for separation factor, which is an essential characteristic of Langmuir isotherm, and can be defined by the following formula [53, 54]:

$$R_L = \frac{1}{1 + K_L C_0} \quad (10)$$

where  $C_0$  stands for the initial concentration, and the value of  $R_L$  is the nature of adsorption which fell between 0 and 1 belong to favorable adsorption.

Freundlich model is used to describe the multilayer adsorption with unequally adsorption sites, and can be expressed by the following formula [53]:

$$\ln q_e = \ln K_F + \frac{1}{n} \ln C_e \quad (11)$$

where  $K_F$  ( $\text{L mg}^{-1}$ ) is the Freundlich constant,  $n$  stands for heterogeneity factor and  $n > 1$  demonstrate the favorable adsorption.

Figure 6b exhibits the adsorption isotherms of MO on to the different photocatalysts. It was found that the adsorption amount  $q_e$  initially increased with increasing concentration of adsorbate and gradually fixed at about 34.09, 38.31 and 44.51  $\text{mg g}^{-1}$  for SNO, LDH, and SNO/LDH, respectively. Table S2 shows the calculated values of parameters based on the isotherms models. For SNO and SNO/LDH, MO adsorption can be well described by Freundlich model (Fig. S2a) due to the higher correlation coefficient than that obtained from the Langmuir model (Fig. S2b). This result suggested that MO adsorption on SNO and SNO/LDH both was heterogeneous. The adsorption isotherm of CoFe-LDH fitted well with the Langmuir model, suggesting that MO adsorption onto CoFe-LDH was monolayer adsorption with identical adsorption sites [50, 55]. Compared with pure SNO and LDH, the adsorption capacity of SNO/LDH was obviously enhanced, which would facilitate the subsequent photocatalytic process. This is because that organic pollutant MO can be concentrated around SNO/LDH by adsorption, and the photocatalytic degradation of MO can be effectively accelerated [56]. Figure S3 shows the MO

discoloration ratio by SNO, LDH, and SNO/LDH. Notably, the MO degradation ratio in dark (21.1%) was much lower than that under visible light irradiation (83.3%), which indicated that photocatalysis was the dominant factor for discoloration of MO.

SNO/CoFe-LDH exhibited excellent magnetic ability, which is important for the recovery of photocatalyst. As shown in Fig. 6c. The coercivity field ( $H_c$ ), remnant magnetization ( $M_r$ ), and saturation magnetization ( $M_s$ ) of SNO/LDH were 26.1551 Oe, 0.329 emu/g, and 10.3226 emu/g, respectively. Moreover, the magnetic hysteresis exhibited a typical S-shaped curve, suggesting the ferrimagnetism character of SNO/LDH. The magnetic separation by a permanent magnet further confirmed the superior magnetic ability of as-synthesized photocatalysts (Fig. 6d), which is beneficial to the recovery of 2D/2D SNO/LDH photocatalysts from aqueous solution.

### Photocatalytic property

The visible-light-driven photocatalytic degradation of MO over as-prepared samples are illustrated in Fig. 7. The blank test of self-degradation of MO was also conducted under visible light irradiation for comparison. Near no degradation of MO was observed without using any photocatalyst, suggesting that the photolysis of the MO in the absence of photocatalysts can be negligible. SNO/CoFe-LDH exhibited enhanced photocatalytic activity than pure SNO and LDH. The MO degradation rate by SNO/CoFe-LDH was up to 83.3% under visible light irradiation for 60 min (Fig. 7a), while those by pure SNO and LDH were 73.3% and 68.8%, respectively, under the same conditions. The enhanced photocatalytic activity of SNO/CoFe-LDH can be attributed to the wider optical absorbance and high separation efficiency of photogenerated charge carriers [57].

To evaluate the degradation rate of MO, the plot of  $\ln(C_0/C)$  against time was analyzed using the pseudo-first-order model [58]:

$$\ln(C_0/C) = kt \quad (12)$$

where  $k$  ( $\text{min}^{-1}$ ) is the kinetic constant of pseudo-first-order,  $C_0$  and  $C$  are stand for concentration of organic dye MO at initial reaction and time  $t$ , respectively. Figure 7b depicts the kinetics fitting curve of MO photodegradation in the presence of as-obtained catalysts. The related pseudo-first-order constants  $k$  were estimated and list in Table S3. SNO/

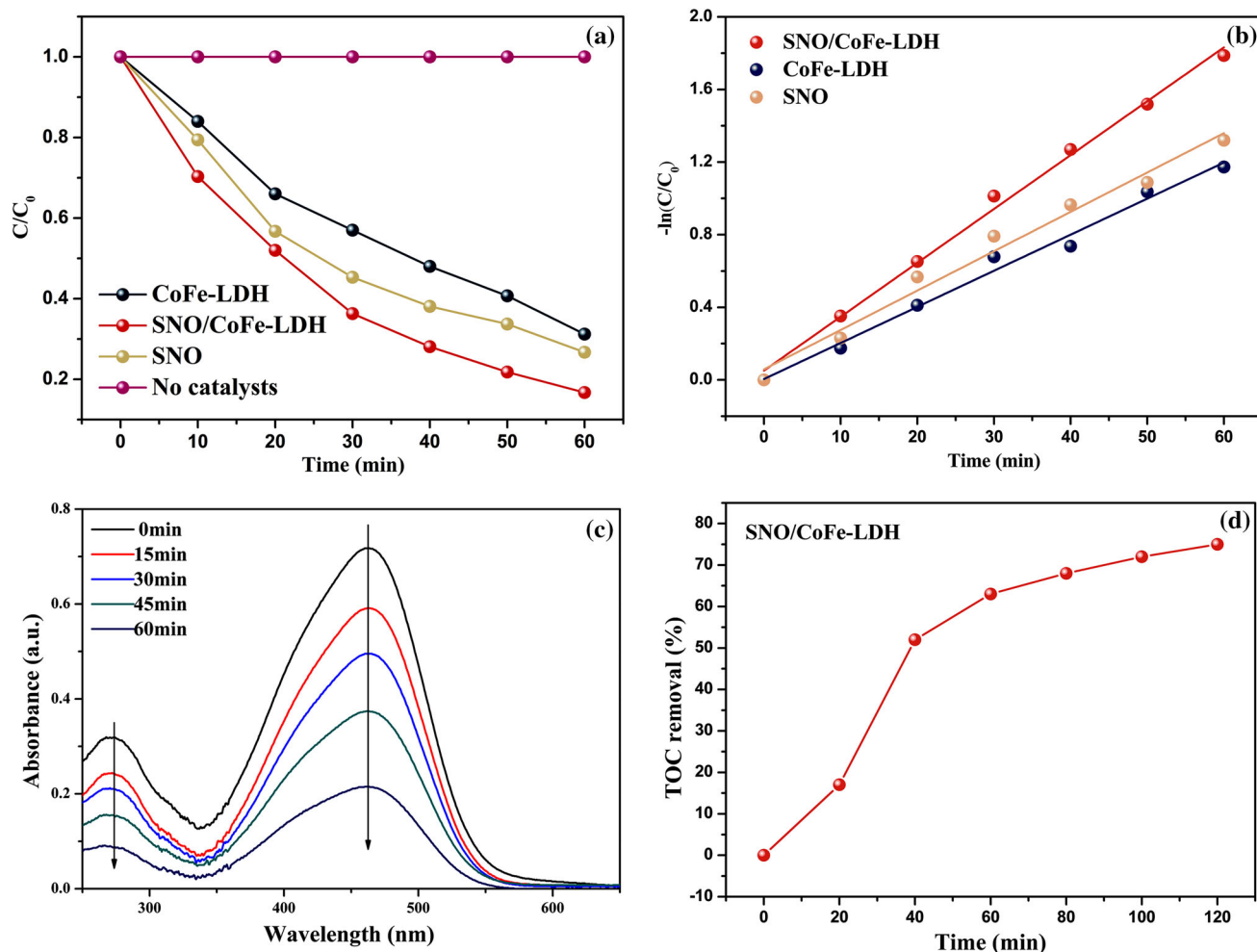


**Figure 7** Photocatalytic degradation (a) and kinetic analysis curves (b) of MO in the presence of SNO, CoFe-LDH and SNO/CoFe-LDH composites (50 mg L<sup>-1</sup> and 80 mL MO, 50 mg photocatalysts). Typical temporal absorbance spectra change of

CoFe-LDH composite had the highest degradation rate constant among three samples, which was around 1.4 times and 1.3 times higher than those of SNO and LDH, respectively.

Methyl orange, as a kind of azo dye, its color mainly results from the interaction of azo function and aromatic species [59]. To elucidate the photocatalytic degradation of MO by SNO/CoFe-LDH, the change of MO absorbance during the photocatalytic process was recorded and the results are shown in Fig. 7c. It can be observed that the absorbance at λ<sub>max</sub> (463 nm) gradually declined as reaction time increased, which means the decreased of the active site (-N=N-) [60, 61]. To further investigate the photocatalytic activity of SNO/CoFe-LDH, the total organic carbon (TOC) concentration of MO solution

was evaluated under room temperature and ambient pressure. As shown in Fig. 7d, the TOC removal efficiency was up to 75% after photocatalytic reaction, which indicated that the organic components can be mostly mineralized into inorganic ones [58]. SNO/CoFe-LDH heterostructure had the superior visible-light-driven photocatalytic capacity, and the corresponding degradation product was environmental-friendly, suggesting the high possibility for further practical application.

The reusability and stability of photocatalysts are vital for practical application. The recycle test of SNO/CoFe-LDH toward the degradation of MO was conducted, and the results were shown in Fig. S4. After three cycles, there is no obvious deactivation of catalyst in the photodegradation of MO, indicating

the good photostability of the SNO/CoFe-LDH heterostructure. The slight decline of degradation activity after four cycles was probably due to the leakage of the catalyst during every time recovered.

### Photocatalytic mechanism

To verify the efficient separation of photoinduced electrons and holes during the photocatalytic reaction, photoluminescence (PL) emission spectra were recorded. As shown in Fig. 8a, the bare SNO had a strong and wide peak centered at around 530 nm under the excitation at 360 nm, while the emission intensity of SNO/CoFe-LDH was obviously decreased. It is suggesting that the recombination of carriers could be efficiently hindered in the heterostructure, which agreed well with the photodegradation performance.

Additionally, to better explore the possible photocatalytic mechanism, the trapping experiments of active species were examined. Herein, some scavengers were added in the photocatalytic system, such as ethylene diamine tetraacetic acid (EDTA, 1 mmol), isopropanol (IPA, 1 mmol), 1,4-benzoquinone (BQ, 1 mmol), for the hole ( $h^+$ ), hydroxyl radical ( $\cdot OH$ ), and superoxide ( $\cdot O^-$ ) scavenger, respectively [12, 62, 63]. As displayed in Fig. 8b, when IPA as a  $\cdot OH$  scavenger was added to the solution, the degradation ratio of MO over the SNO/CoFe-LDH was not obviously decreased, implying that few  $\cdot OH$  participated in effective photodegradation. When EDTA was added in the system, the rate of

discoloration was apparently decreased, indicating that the  $h^+$  was important for degradation of MO during the reaction proceeding. The similar decrease occurred when BQ was added. Compared with the degradation ratio in no scavenger experiment, the remarkable inhabitation in presence of  $\cdot O^-$  scavenger can be ascribed to the fact that superoxide was the main active radical in photocatalytic reaction. These observations clearly indicate that the photogenerated holes and  $\cdot O^-$  were mainly active species responsible for degradation of MO over SNO/CoFe-LDH.

Figure 9 schematically shows the improved photocatalytic performance of SNO/CoFe-LDH and the corresponding transfer of electro-hole pairs between SNO and LDH. The unique 2D–2D SNO/CoFe-LDH microstructure can provide more exposed active sites, and thus can promote adsorption and photocatalysis simultaneously. On the other hand, the energy band structures of SNO and LDH matched well and thus can improve photocatalytic activity. It is noted that the  $E_{CB}$  of LDH ( $-1.32$  eV) was more negative than that of SNO ( $-0.96$  eV), while the  $E_{VB}$  of SNO ( $1.57$  eV) was more positive than that of LDH ( $0.86$  eV). Therefore, the photoinduced electrons could easily transport from the conduction band (CB) of LDH to the CB of SNO, and the photogenerated holes from the valence band (VB) of SNO would transport to that of LDH at the same time. The improved transferred and separated efficiency of photoinduced charge carriers can lead to high photocatalytic performance. Besides, the reducibility of

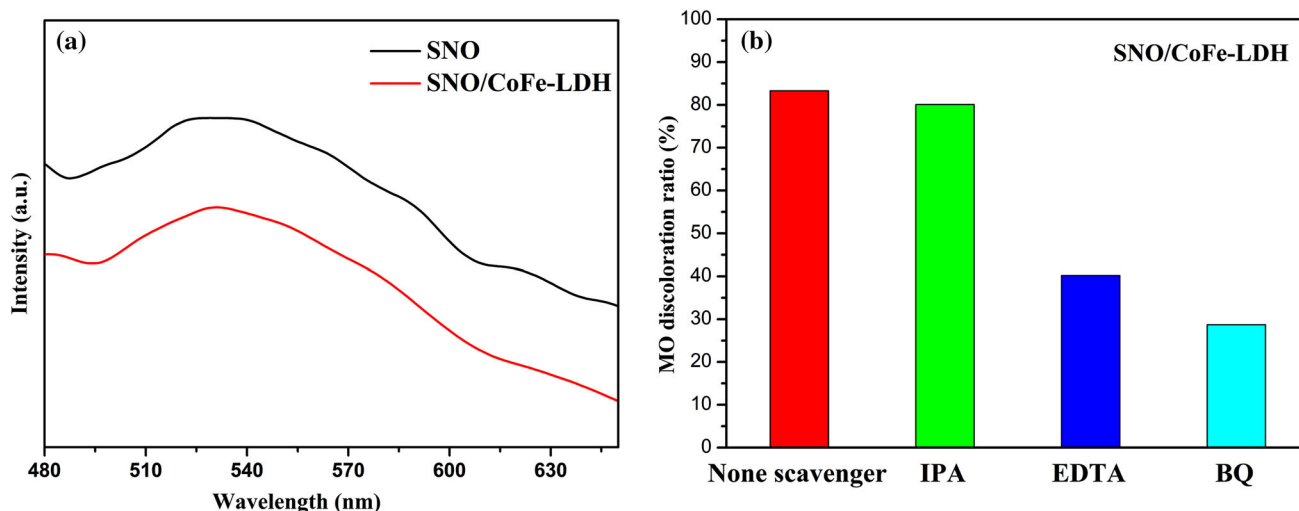


**Figure 8** Photoluminescence spectra (PL) of pure SNO and SNO/CoFe-LDH heterostructure under the excitation wavelength of 360 nm (a), trapping experiment of the active species for the degradation of MO over SNO/CoFe-LDH heterostructure (b).

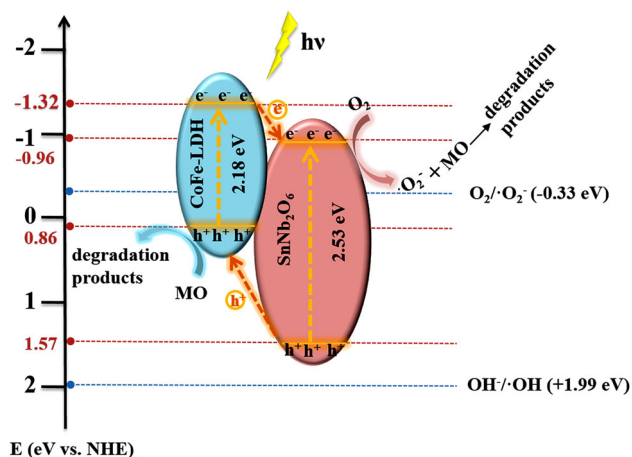


**Figure 9** Possible schematic diagram of the photocatalytic mechanism for as-prepared SNO/CoFe-LDH heterostructures under the excitation of simulate visible light.

SNO was higher than  $O_2$  due to the more negative CB potential of SNO ( $-0.96$  eV) than the standard redox potential  $E^0$  ( $O_2/\cdot O_2^-$ ,  $-0.33$  eV), and thus the superoxide radicals ( $\cdot O_2^-$ ) can be generated during the charge migration. These radicals with strong oxidizing properties can oxidize MO molecules into small molecules such as  $CO_2$  and  $H_2O$  [64]. Meanwhile, MO can be oxidized directly by the holes in the VB of LDH that had great oxidizing ability. Furthermore, the synergy effect between adsorption and photocatalytic also played a vital role in process of degradation dyes. The enrichment effect of MO provide by adsorption benefited the photocatalytic degradation of MO [56]. Thus, we believed that the performance of photocatalytic of 2D–2D SNO/CoFe-LDH heterojunctions has been enhanced mainly attributed to the unique architecture, improved charge transfer efficiency and light-harvesting ability, and synergy adsorption–photocatalysis effect.

## Conclusion

In summary, we have successfully fabricated a novel 2D–2D magnetic SNO/CoFe-LDH heterojunctions via a simple hydrothermal method. This nanocomposite exhibited excellent photocatalytic performance for MO degradation than either pure SNO or CoFe-LDH under the same conditions. The formation of a hybrid nanojunction between SNO and CoFe-LDH was crucial for the separation efficiency of photo-generated charge carries. In addition, superoxide

radicals and holes were demonstrated the main active species for MO degradation in the presence of SNO/CoFe-LDH. Furthermore, SNO/CoFe-LDH photocatalyst held quick magnetic response under an external magnetic, which means that SNO/CoFe-LDH can be easily recovered after photocatalysis. This work provides some insights into design and fabrication of magnetic 2D–2D nanostructure photocatalysts for wastewater treatment.

## Acknowledgements

This work was supported by National Natural Science Foundation of China (Grant No. 51672110).

## Compliance with ethical standards

**Conflict of interest** All authors declare that they have no conflict of interest.

**Electronic supplementary material:** The online version of this article (<https://doi.org/10.1007/s10853-018-2810-6>) contains supplementary material, which is available to authorized users.

## References

- [1] Li HJ, Zhou Y, Tu WG, Ye JH, Zou ZG (2015) State-of-the-Art progress in diverse heterostructured photocatalysts toward promoting photocatalytic performance. *Adv Funct Mater* 25:998–1013
- [2] Moniz SJA, Shevlin SA, Martin DJ, Guo ZX, Tang JW (2015) Visible-light driven heterojunction photocatalysts for water splitting—a critical review. *Energy Environ Sci* 8:731–759
- [3] Tong H, Ouyang SX, Bi YP, Umezawa N, Oshikiri M, Ye JH (2012) Nano-photocatalytic materials: possibilities and challenges. *Adv Mater* 24:229–251
- [4] Zhou HL, Qu YQ, Zeid T, Duan XF (2012) Towards highly efficient photocatalysts using semiconductor nanoarchitectures. *Energy Environ Sci* 5:6732–6743
- [5] Pan CS, Takata T, Kumamoto K, Ma SSK, Ueda K, Minegishi T, Nakabayashi M, Matsumoto T, Shibata N, Ikumura Y (2016) Band engineering of perovskite-type transition metal oxynitrides for photocatalytic overall water splitting. *J Mater Chem A* 4:4544–4552
- [6] Zhang DQ, Wen MC, Zhang SS, Liu PJ, Zhu W, Li GS, Li HX (2014) Au nanoparticles enhanced rutile  $TiO_2$  nanorod

- bundles with high visible-light photocatalytic performance for NO oxidation. *Appl Catal B: Environ* 147:610–616
- [7] Zhang K, Guo LJ (2013) Metal sulphide semiconductors for photocatalytic hydrogen production. *Catal Sci Technol* 3:1672–1690
- [8] Yang C, Huang Y, Li F, Li T (2016) One-step synthesis of Bi<sub>2</sub>WO<sub>6</sub>/TiO<sub>2</sub> heterojunctions with enhanced photocatalytic and superhydrophobic property via hydrothermal method. *J Mater Sci* 51:1032–1042. <https://doi.org/10.1007/s10853-015-9433-y>
- [9] Liang SJ, Liang RW, Wen LR, Yuan RS, Wu L, Fu XZ (2012) Molecular recognitive photocatalytic degradation of various cationic pollutants by the selective adsorption on visible light-driven SnNb<sub>2</sub>O<sub>6</sub> nanosheet photocatalyst. *Appl Catal B: Environ* 125:103–110
- [10] Zhu SY, Liang SJ, Bi JH, Liu MH, Zhou LM, Wu L, Wang XX (2016) Photocatalytic reduction of CO<sub>2</sub> with H<sub>2</sub>O to CH<sub>4</sub> over ultrathin SnNb<sub>2</sub>O<sub>6</sub> 2D nanosheets under visible light irradiation. *Green Chem* 18:1355–1363
- [11] Liang SJ, Zhu SY, Chen Y, Wu WM, Wang XC, Wu L (2012) Rapid template-free synthesis and photocatalytic performance of visible light-activated SnNb<sub>2</sub>O<sub>6</sub> nanosheets. *J Mater Chem* 22:2670–2678
- [12] Jin Y, Jiang DL, Li D, Chen M (2017) Construction of ultrafine TiO<sub>2</sub> nanoparticle and SnNb<sub>2</sub>O<sub>6</sub> nanosheet 0D-2D heterojunctions with abundant interfaces and significantly improved photocatalytic activity. *Catal Sci Technol* 7:2308–2317
- [13] Zhang ZY, Jiang DL, He MQ, Chen M (2016) Construction of SnNb<sub>2</sub>O<sub>6</sub> nanosheet/g-C<sub>3</sub>N<sub>4</sub> nanosheet two-dimensional heterostructures with improved photocatalytic activity: synergistic effect and mechanism insight. *Appl Catal B: Environ* 183:113–123
- [14] Liang YT, Vijayan BK, Lyandres O, Gray KA, Hersam MC (2012) Effect of dimensionality on the photocatalytic behavior of carbon-titania nanosheet composites: charge transfer at nanomaterial interfaces. *J Phys Chem Lett* 3:1760–1765
- [15] Sun J, Zhang H, Guo LH, Zhao LX (2013) Two-dimensional interface engineering of a titania-graphene nanosheet composite for improved photocatalytic activity. *ACS Appl Mater Interface* 5:13035–13041
- [16] Yang J, Voiry D, Ahn SJ, Kang D, Kim AY, Chhowalla M, Shin HS (2013) Two-dimensional hybrid nanosheets of tungsten disulfide and reduced graphene oxide as catalysts for enhanced hydrogen evolution. *Angew Chem Int Ed* 52:13751–13754
- [17] Chakraborty J, Sengupta S, Dasgupta S, Chakraborty M, Ghosh S, Mallik S, Das KL, Basu D (2012) Determination of trace level carbonate ion in Mg–Al layered double hydroxide: its significance on the anion exchange behaviour. *J Ind Eng Chem* 18:2211–2216
- [18] Mohapatra L, Parida K (2016) A review on the recent progress, challenges and perspective of layered double hydroxides as promising photocatalysts. *J Mater Chem A* 4:10744–10766
- [19] Zhou YJ, Zhang LX, Huang WM, Kong QL, Fan XQ, Wang M, Shi JL (2016) N-doped graphitic carbon-incorporated g-C<sub>3</sub>N<sub>4</sub> for remarkably enhanced photocatalytic H<sub>2</sub> evolution under visible light. *Carbon* 99:111–117
- [20] Song F, Hu XL (2014) Exfoliation of layered double hydroxides for enhanced oxygen evolution catalysis. *Nat Commun* 5:4477
- [21] Shao MF, Wei M, Evans DG, Duan X (2011) Magnetic-field-assisted assembly of CoFe layered double hydroxide ultrathin films with enhanced electrochemical behavior and magnetic anisotropy. *Chem Commun* 47:3171–3173
- [22] Gong JL, Wang B, Zeng GM, Yang CP, Niu CG, Niu QY, Zhou WJ, Liang Y (2009) Removal of cationic dyes from aqueous solution using magnetic multi-wall carbon nanotube nanocomposite as adsorbent. *J Hazard Mater* 164:1517–1522
- [23] Abellán G, Carrasco JA, Coronado E, Romero J, Varela M (2014) Alkoxide-intercalated CoFe-layered double hydroxides as precursors of colloidal nanosheet suspensions: structural, magnetic and electrochemical properties. *J Mater Chem C* 2:3723–3731
- [24] Kim SJ, Lee Y, Lee DK, Lee JW, Kang JK (2014) Efficient Co–Fe layered double hydroxide photocatalysts for water oxidation under visible light. *J Mater Chem A* 2:4136–4139
- [25] Zhang XM, Wang YL, Dong SY, Li MG (2015) Dual-site polydopamine spheres/CoFe layered double hydroxides for electrocatalytic oxygen reduction reaction. *Electrochim Acta* 170:248–255
- [26] Ma KY, Cheng JP, Zhang J, Li M, Liu F, Zhang XB (2016) Dependence of Co/Fe ratios in Co–Fe layered double hydroxides on the structure and capacitive properties. *Electrochim Acta* 198:231–240
- [27] Ma XD, Ma WX, Jiang DL, Li D, Meng SC, Chen M (2017) Construction of novel WO<sub>3</sub>/SnNb<sub>2</sub>O<sub>6</sub> hybrid nanosheet heterojunctions as efficient Z-scheme photocatalysts for pollutant degradation. *J Colloid Interface Sci* 506:93–101
- [28] Lu L, Li J, Ng DHL, Yang P, Song P, Zuo M (2017) Synthesis of novel hierarchically porous Fe<sub>3</sub>O<sub>4</sub>@MgAl–LDH magnetic microspheres and its superb adsorption properties of dye from water. *J Ind Eng Chem* 46:315–323
- [29] Rives V (2002) Characterisation of layered double hydroxides and their decomposition products. *Mater Chem Phys* 75:19–25

- [30] Ao YH, Wang DD, Wang PF, Wang C, Hou J, Qian J (2016) Enhanced photocatalytic properties of the 3D flower-like Mg–Al layered double hydroxides decorated with  $\text{Ag}_2\text{CO}_3$  under visible light illumination. *Mater Res Bull* 80:23–29
- [31] Chen FF, Wu X, Bu R, Yang F (2017) Co–Fe hydrotalcites for efficient removal of dye pollutants via synergistic adsorption and degradation. *RSC Adv* 74:1945–41954
- [32] Jawad A, Li YB, Lu XY, Chen ZQ, Liu WD, Yin GH (2015) Controlled leaching with prolonged activity for Co-LDH supported catalyst during treatment of organic dyes using bicarbonate activation of hydrogen peroxide. *J Hazard Mater* 289:165–173
- [33] Ganiyu SO, Le TXH, Bechelany M, Esposito G, van Hullebusch ED, Oturan MA, Certin M (2017) A hierarchical CoFe-layered double hydroxide modified carbon-felt cathode for heterogeneous electro-Fenton process. *J Mater Chem A* 5:3655–3666
- [34] Li Y, Zhang L, Xiang X, Yan DP, Li F (2014) Engineering of ZnCo-layered double hydroxide nanowalls toward high-efficiency electrochemical water oxidation. *J Mater Chem A* 2:13250–13258
- [35] Zhao JW, Chen JL, Xu SM, Shao MF, Yan DP, Wei M, Evans DG, Duan X (2013) CoMn-layered double hydroxide nanowalls supported on carbon fibers for high-performance flexible energy storage devices. *J Mater Chem A* 1:8836–8843
- [36] Lavat AE, Baran EJ (2003) IR-spectroscopic characterization of  $\text{A}_2\text{BB}'\text{O}_6$  perovskites. *Vib Spectrosc* 32:167–174
- [37] Newman SP, Jones W (1998) Synthesis, characterization and applications of layered double hydroxides containing organic guests. *New J Chem* 22:105–115
- [38] Han LL, Dong CQ, Zhang C, Gao YL, Zhang J, Gao H, Wang Y, Zhang ZH (2017) Dealloying-directed synthesis of efficient mesoporous CoFe-based catalysts towards the oxygen evolution reaction and overall water splitting. *Nanoscale* 9:16467–16475
- [39] Villarroel-Rocha J, Barrera D, Sapag K (2014) Introducing a self-consistent test and the corresponding modification in the Barrett, Joyner and Halenda method for pore-size determination. *Microporous Mesoporous Mater* 200:68–78
- [40] Yang J, Yu C, Fan XM, Ling Z, Qiu JS, Gogotsi Y (2013) Facile fabrication of MWCNT-doped NiCoAl-layered double hydroxide nanosheets with enhanced electrochemical performances. *J Mater Chem A* 1:1963–1968
- [41] Yu C, Yang J, Zhao C, Fan X, Wang G, Qiu J (2014) Nanohybrids from NiCoAl-LDH coupled with carbon for pseudocapacitors: understanding the role of nano-structured carbon. *Nanoscale* 6:3097–3104
- [42] Yu C, Han X, Liu Z, Zhao C, Huang H, Yang J, Niu Y, Qiu J (2018) An effective graphene confined strategy to construct active edge sites-enriched nanosheets with enhanced oxygen evolution. *Carbon* 126:437–442
- [43] Atuchin VV, Kalabin IE, Kesler VG, Pervukhina NV (2005) Nb 3d and O 1 s core levels and chemical bonding in niobates. *J Electron Spectrosc* 142:129–134
- [44] Li QY, Kako T, Ye JH (2011) Facile ion-exchanged synthesis of  $\text{Sn}^{2+}$  incorporated potassium titanate nanoribbons and their visible-light-responded photocatalytic activity. *Int J Hydrog Energy* 36:4716–4723
- [45] Zhang GH, Lin BZ, Qiu YQ, He LW, Chen YL, Gao BF (2015) Highly efficient visible-light-driven photocatalytic hydrogen generation by immobilizing CdSe nanocrystals on ZnCr-layered double hydroxide nanosheets. *Int J Hydrog Energy* 40:4758–4765
- [46] Nayak S, Mohapatra L, Parida K (2015) Visible light-driven novel  $\text{g-C}_3\text{N}_4/\text{NiFe-LDH}$  composite photocatalyst with enhanced photocatalytic activity towards water oxidation and reduction reaction. *J Mater Chem A* 3:18622–18635
- [47] Liu Q, Ma JF, Wang K et al (2017) BiOCl and  $\text{TiO}_2$  deposited on exfoliated ZnCr-LDH to enhance visible-light photocatalytic decolorization of Rhodamine B. *Ceram Int* 43:5751–5758
- [48] Peng C, Gao L (2008) Optical and photocatalytic properties of spinel  $\text{ZnCr}_2\text{O}_4$  nanoparticles synthesized by a hydrothermal route. *J Am Ceram Soc* 91:2388–2390
- [49] Elaziouti A, Laouedj N, Bekka A, Vannier R-N (2015) Preparation and characterization of p–n heterojunction  $\text{CuBi}_2\text{O}_4/\text{CeO}_2$  and its photocatalytic activities under UVA light irradiation. *J KSU Sci* 27:120–135
- [50] Lu L, Li J, Yu J, Song P, Ng DHL (2016) A hierarchically porous  $\text{MgFe}_2\text{O}_4/\gamma\text{-Fe}_2\text{O}_3$  magnetic microspheres for efficient removals of dye and pharmaceutical from water. *Chem Eng J* 283:524–534
- [51] Ho YS, Mckay G (1999) Pseudo-second order model for sorption processes. *Process Biochem* 34:451–465
- [52] Azizian S (2004) Kinetic models of sorption: a theoretical analysis. *J Colloid Interface Sci* 276:47–52
- [53] Crini G, Peindy HN, Gimbert F, Robert C (2007) Removal of CI Basic Green 4 (Malachite Green) from aqueous solutions by adsorption using cyclodextrin-based adsorbent: kinetic and equilibrium studies. *Sep Purif Technol* 53:97–110
- [54] Ofomaja AE, Ho YS (2007) Equilibrium sorption of anionic dye from aqueous solution by palm kernel fibre as sorbent. *Dyes Pigment* 74:60–66
- [55] Shuang CD, Li PH, Li AM, Zhou Q, Zhang MC, Zhou Y (2012) Quaternized magnetic microspheres for the efficient removal of reactive dyes. *Water Res* 46:4417–4426
- [56] Xu HY, Wu LC, Zhao H, Jin LG, Qi SY (2015) Synergistic effect between adsorption and photocatalysis of metal-free

- g-C<sub>3</sub>N<sub>4</sub> derived from different precursors. PLoS ONE 10:e0142616
- [57] Yuan XY, Li WY (2017) Graphitic-C<sub>3</sub>N<sub>4</sub> modified ZnAl-layered double hydroxides for enhanced photocatalytic removal of organic dye. Appl Clay Sci 138:107–113
- [58] Li HY, Li J, Xu CC, Yang P, Ng DHL, Song P, Zuo M (2017) Hierarchically porous MoS<sub>2</sub>/CoAl-LDH/HCF with synergistic adsorption-photocatalytic performance under visible light irradiation. J Alloy Compd 698:852–862
- [59] Khataee AR, Pons MN, Zahraa O (2009) Photocatalytic degradation of three azo dyes using immobilized TiO<sub>2</sub> nanoparticles on glass plates activated by UV light irradiation: influence of dye molecular structure. J Hazard Mater 168:451–457
- [60] Bahrami M, Jafar Hoseini S (2018) Simultaneous formation of platinum-based nanocatalysts and degradation of dyes at oil/water interface: comparative morphological and kinetic studies. Appl Organomet Chem 32:e3920
- [61] Hu KH, Hu XG, Xu YF, Sun JD (2010) Synthesis of nano-MoS<sub>2</sub>/TiO<sub>2</sub> composite and its catalytic degradation effect on methyl orange. J Mater Sci 45:2640–2648. <https://doi.org/10.1007/s10853-010-4242-9>
- [62] Li H, Li W, Wang F, Liu X, Ren C (2017) Fabrication of two lanthanides co-doped Bi<sub>2</sub>MoO<sub>6</sub> photocatalyst: selection, design and mechanism of Ln<sub>1</sub>/Ln<sub>2</sub> redox couple for enhancing photocatalytic activity. Appl Catal B 217:378–387
- [63] Teng W, Li X, Zhao Q, Zhao J, Zhang D (2012) In situ capture of active species and oxidation mechanism of RhB and MB dyes over sunlight-driven Ag/Ag<sub>3</sub>PO<sub>4</sub> plasmonic nanocatalyst. Appl Catal B 125:538–545
- [64] Thennarasu G, Sivasamy A (2015) Synthesis and characterization of nanolayered ZnO/ZnCr<sub>2</sub>O<sub>4</sub> metal oxide composites and its photocatalytic activity under visible light irradiation. J Chem Technol Biotechnol 90:514–524